



Contents lists available at ScienceDirect

## Arabian Journal of Chemistry

journal homepage: [www.ksu.edu.sa](http://www.ksu.edu.sa)

# Synthesis of $Ti_3C_2T_x$ nanosheets / ZnO nanowires composite material for $NO_2$ gas sensing

Jiyun Gao<sup>a,b,c</sup>, Youyou Yin<sup>a</sup>, Yongjing Guo<sup>b</sup>, Lijuan Jia<sup>a</sup>, Futing Xia<sup>a</sup>, Chenhui Liu<sup>a,\*</sup>, Ming Hou<sup>b</sup>, Fang Wang<sup>a,\*</sup>

<sup>a</sup> School of Chemistry and Environment, Yunnan Minzu University, Kunming 650093, China

<sup>b</sup> Faculty of Metallurgical and Energy Engineering, Kunming University of Science and Technology, Kunming 650093, China

<sup>c</sup> Laboratory of Environmental Functional Materials of Yunnan Province Education Department, School of Chemistry and Environment, Yunnan Minzu University, Kunming, 650500, China

## ARTICLE INFO

## Keywords:

ZnO nanowires  
 $Ti_3C_2T_x/ZnO$   
 $NO_2$  gas sensing  
 Electrostatic self-assemble

## ABSTRACT

$NO_2$  is a toxic gas that poses a significant threat to the environment and human health. In this work, one-dimensional ZnO nanowires and two-dimensional layered titanium carbide ( $Ti_3C_2T_x$ ) have been prepared by hydrothermal and selective chemical etching methods, respectively. The  $Ti_3C_2T_x/ZnO$  composites are synthesized by electrostatic self-assembly method. The characterization results indicate that the ZnO nanowires are uniformly dispersed on the surface of layered  $Ti_3C_2T_x$  to form a heterostructure. Meanwhile, the gas sensitive performance of  $Ti_3C_2T_x/ZnO$  composite material is investigated and compared with that of pure  $Ti_3C_2T_x$ . The results reveal that the composite exhibits a high selectivity as well as sensitivity with a response value ( $S = R_g/R_a$ ) of 18.66 to 100 ppm  $NO_2$  at 250 °C, which is 4.3 times higher than that of pure  $Ti_3C_2T_x$ . This proves that the prepared composite material is an effective sensing material for detecting  $NO_2$  gas.

## 1. Introduction

The rapid global industrialization has led to severe environmental degradation, especially air pollution, which poses a serious risk to human health (Bhowmick et al., 2022; Keerthana et al., 2022).  $NO_2$  is one of the most harmful gases originating from fuel combustion and automobile exhaust emissions, which not only produces acid rain but also causes serious atmospheric pollution. In particular, long-term exposure to ppm-level  $NO_2$  can cause lung inflammation, asthma, tissue hypoxia, and other diseases in humans (Yuan et al., 2018; Liu et al., 2022; Fan et al., 2022). Therefore, it is crucial to develop a highly sensitive and selective  $NO_2$  gas sensor that can detect low-concentration (ppb-level)  $NO_2$  (Shuvo et al., 2020). The resistive Metal-Oxide-Semiconductor (MOS)-based gas sensors based on the gas-solid reaction principle are widely used for detecting low-concentration  $NO_2$  gas because of their low cost, simple synthesis route, portability, and high stability (Tetrycz et al., 2004). The commonly used metal oxides in the wide-band-gap MOS gas sensors are ZnO (Qiu et al., 2014),  $SnO_2$  (Wei et al., 2004),  $WO_3$  (Kanda et al., 2005),  $TiO_2$  (Li et al., 2018),  $Co_3O_4$ ,  $W_{18}O_{49}$  and CuO. However, the application of these sensors is limited by

several problems, such as high operating temperature, long response time, poor selectivity, and broad spectral response to gases with similar redox characteristics (Chen et al., 2018; Zheng et al., 2021). To overcome these problems, it is essential to improve the semiconducting property of metal oxide by combining it with a two-dimensional (2D) material, which can increase the effective contact area between the sensitive material and gas surface, accelerating the free charge transfer during the gas-solid reaction process (Tetrycz et al., 2004; Yang et al., 2021; Wang et al., 2021). This is a feasible method to improve the selectivity and reduce the operating temperature of the  $NO_2$  gas sensor.

MXenes are an emerging family of 2D transition metal carbides and/or nitrides, which are generally synthesized by chemical etching of the A element in the MAX phases. They have a graphene-like 2D layered structure, and their general chemical composition can be expressed as  $M_{n+1}X_nT_x$  ( $n = 1-3$ ), where M is an early transition metal such as Ti, V, Nb, and Ta, X is C or N, and  $T_x$  represents the surface functional groups such as -OH, -O, and -F (Gogotsi et al., 2019; Naguib et al., 2012; Naguib et al., 2011). Compared to the other 2D materials, MXene with a large specific surface area and excellent electrical conductivity exhibits (Orangi et al., 2020). Furthermore, a large number of functional groups

\* Corresponding authors.

E-mail addresses: [liu-chenhui@hotmail.com](mailto:liu-chenhui@hotmail.com) (C. Liu), [wfk0202@126.com](mailto:wfk0202@126.com) (F. Wang).

<https://doi.org/10.1016/j.arabjc.2024.105776>

Received 5 December 2023; Accepted 2 April 2024

Available online 16 April 2024

1878-5352/© 2024 The Author(s). Published by Elsevier B.V. on behalf of King Saud University. This is an open access article under the CC BY license (<http://creativecommons.org/licenses/by/4.0/>).

are present on the surface of MXenes, which can provide abundant active sites for gas adsorption and surface reaction. In addition, owing to their unique layered structure, MXenes are also widely used in photocatalysis, energy storage (Naguib et al., 2011; Fan et al., 2018; Orangi et al., 2020), electromagnetic shielding (Li et al., 2021), etc. Until now, several kinds of MXenes have been successfully synthesized by etching and exfoliating various MAX phases, such as  $Ti_3C_2T_x$ ,  $V_2C$ ,  $Nb_2C$ ,  $Nb_4C_3$ ,  $Ti_4N_3$ , and  $Mo_2C$  (Liu et al., 2019; Lee et al., 2019; Halim et al., 2016). However, pure 2D MXenes have some limitations as a gas sensing material, such as low sensitivity, poor selectivity, and slow response and recovery.

Notably, the gas-sensing performance of MXene such as 2D  $Ti_3C_2T_x$  can be enhanced by combining it with ZnO to form a composite gas sensitive material. This strategy can fully utilize the excellent gas-sensitive characteristics of ZnO as well as the large specific surface area and multiple efficient conductive channels of 2D  $Ti_3C_2T_x$ . In this work, the  $Ti_3C_2T_x/ZnO$  composites are synthesized by using uniform ZnO nanowires and  $Ti_3C_2T_x$  via the electrostatic self-assembly method. The results reveal that the  $Ti_3C_2T_x/ZnO$  composites exhibit excellent  $NO_2$  gas sensing properties, and the fabricated sensor based on the composites displays a good response of 18.66 to 100 ppm  $NO_2$  with outstanding selectivity. Additionally, the mechanism for enhancing the sensing response is explored. The enhanced sensing properties of the ZnO/MXene composite material with the two-dimensional conductive network indicate its immense potential in gas sensing applications.

## 2. Experimental

### 2.1. Raw materials and equipment

The chemicals used were  $Zn(NO_3)_2 \cdot 6H_2O$ , NaOH,  $C_6H_{12}N_4$  (HMTA), NaF,  $CH_3CH_2OH$ , LiF (purity  $\geq 99\%$ , Aladdin's reagent), HCl,  $Ti_3AlC_2$  MAX powder, and polydiallyl dimethyl ammonium chloride (PDDA, Aladdin's reagent). Deionized water was used throughout the experiment.

The experimental equipment included JJ1023BC electronic scale, TG16-WS centrifugal machine, SK330BT supersonic cleaner, DHG-9145A drying oven, XinYi-10 freeze drier, OTF-1200X tube furnace, DF-101S magnetic stirrer, and SD101 fourchannel gas sensitive measuring instrument.

### 2.2. Sample Preparation

#### (1) Synthesis of one-dimensional ZnO nanowires

The ZnO nanowires were fabricated by a hydrolysis approach. Firstly, solution A was obtained by dissolving 1.19 g  $Zn(NO_3)_2 \cdot 6H_2O$  and 0.169 g NaOH in 40 ml distilled water under continuous stirring. Then, 0.28 g  $C_6H_{12}N_4$  (HMTA) and 0.84 g NaF were dissolved in 40 ml distilled water to obtain solution B. Next, the solutions A and B were mixed for 0.5 h through magnetic stirring. Subsequently, the mixed solution was transferred to a polytetrafluoroethylene (PTFE)-lined autoclave, which was then heated at  $120^\circ C$  in a constant-temperature furnace for 10 h. The white precipitate was collected, then. The precipitate was separated by centrifugation and cleaned with deionized water for several times until the solution was neutral. Finally, the samples were dried in a drying oven at  $80^\circ C$  for 8–10 h to obtain a white powder for further use (Wang et al., 2004). The one-dimensional (1D) ZnO nanowires were obtained by heating the dried sample to  $400^\circ C$  at a rate of  $5^\circ C/min$  in a tube furnace and maintaining it for 2 h.

#### (2) Preparation of 2D $Ti_3C_2T_x$

Firstly, 1 g LiF powder was dissolved in 10 mL HCl with a concentration of 9 mol/L and stirred at room temperature for 30 min. In an ice bath, 1 g  $Ti_3AlC_2$  MAX powder was slowly added to the above solution to

avoid initial overheating of the solution due to exothermic reaction, and then the solution was transferred to an oil bath at  $35^\circ C$  and continuously stirred for 24 h (Li et al., 2018; Kim et al., 2018; He et al., 2021; Pei et al., 2021). Then, the powder was dispersed for 1 h to obtain  $Ti_3C_2T_x$ . After centrifugation at 3500 rpm for 5 min, the supernatant was discarded, and the precipitate was washed with deionized water to a pH of 6. Finally, the sample was vacuum dried for 10 h to obtain the  $Ti_3C_2T_x$  powder.

#### (3) Fabrication of $Ti_3C_2T_x/ZnO$ composites by electrostatic self-assembly

Firstly, 1 g of the synthesized 1D ZnO nanowires was dispersed in 300 mL of 5% PDDA, followed by ultrasonication for 3 h. After filtration, the PDDA-modified ZnOPDDA was washed with deionized water and dried for 12 h in a drying oven at  $70^\circ C$ . Subsequently, 1 g PDDA-modified ZnO powder was dissolved in 10.00 mL deionized water. Then, a certain amount of  $Ti_3C_2T_x$  was added, and the powder was vigorously stirred under the protection of argon gas for 10 h. Here, the composite material samples with the  $Ti_3C_2T_x$  mass fraction of 14%, 25%, and 40% are denoted as M1, M2, and M3, and the pure  $Ti_3C_2T_x$  MXene is called M.

### 2.3. Characterization of $Ti_3C_2T_x/ZnO$ composites

The prepared  $Ti_3C_2T_x/ZnO$  composites were characterized by X-ray diffraction (XRD; A25X, Bruker, Germany), scanning electron microscopy (SEM; NOVA NANOSEM –450, FEI, USA), high-resolution transmission electron microscopy (HRTEM, JEM-2100Plus, JEOL Ltd., Japan), X-ray photoelectron spectroscopy (XPS; Thermo Fisher, Thermo Scientific, USA), and Brunauer-Emmett-Teller (BET) surface area analysis (BELSORP, Microtrac MRB, Japan).

### 2.4. Fabrication of gas sensing device

An appropriate amount of  $Ti_3C_2T_x/ZnO$  was placed in a beaker, and a small amount of pre-prepared organic solvent was added to form a thick liquid slurry. The slurry sample was printed on an alumina matrix by using screen printing to form a material film with a thickness of 5–10  $\mu m$ . Then, these alumina matrixes were dried at  $70^\circ C$  for 40 min and calcined at  $350^\circ C$  for 2 h, followed by heat treatment at  $550^\circ C$  for 2 h to enhance the mechanical bond of nanowires in the films (Hou et al., 2021). Finally, a thick porous film was formed for gas-sensing performance test.

### 2.5. Gas-sensing performance test

The gas-sensing performance of the samples was evaluated using a four-channel testing device (SD101, Wuhan Huachuang Ruike Tech. Co. Ltd., Wuhan, China). The test system included a computer, a gas flow controller, and a four-channel test chamber. During the test, the test chip was placed in a closed chamber filled with air. When the resistance showed a stable baseline, different working temperatures and different concentrations of target gas were set. At least three samples of each type were tested, and the average values were calculated. The gas response can be evaluated as follows:

$$S = R_g/R_a$$

where  $R_a$  is the sample resistance in air, and  $R_g$  is the sample resistance in the presence of  $NO_2$  gas.

### 3. Results and discussion

#### 3.1. Morphology and composition

The crystal structure of the prepared samples was examined by XRD, and the results are shown in Fig. 1. It can be seen that the ZnO sample has narrow and sharp characteristic peaks without any impurity peak. The diffraction peaks are located at  $31.8^\circ$ ,  $34.3^\circ$ ,  $36.35^\circ$ ,  $47.54^\circ$ ,  $56.53^\circ$ ,  $62.92^\circ$ ,  $67.9^\circ$ , and  $69.1^\circ$ , which correspond to the (100), (002), (101), (102), (103), (112), and (201) crystal planes, respectively (Keerthana et al., 2022; Gong et al., 2014; Srinivasan et al., 2022) in accordance with the Standard JCPDS Card No. 36–1451. The XRD results suggest that the prepared ZnO sample is a typical feldspathic zincite structure. The diffraction peaks of  $\text{Ti}_3\text{AlC}_2$  precursor are in good agreement with the Standard JCPDS Card No. 52–0875 (Li et al., 2019), and there are no impurity peaks, which proves that  $\text{Ti}_3\text{AlC}_2$  is of high purity. The typical characteristic peaks at  $9.65^\circ$  and  $39.13^\circ$  correspond to the (002) and (104) crystal planes, respectively. However, these diffraction peaks of  $\text{Ti}_3\text{AlC}_2$  precursor are not observed in the spectra of pure  $\text{Ti}_3\text{C}_2\text{T}_x$  and composite samples M1, M2 and M3, while the strong characteristic peak corresponding to (002) plane of  $\text{Ti}_3\text{C}_2\text{T}_x$  appears at  $6.9^\circ$ . This indicates that through selective etching of  $\text{Ti}_3\text{AlC}_2$  precursor by LiF + HCl solution,  $\text{Ti}_3\text{C}_2\text{T}_x$  with high purity has been successfully prepared. Comparing the XRD patterns of composite materials M1, M2 and M3 with those of pristine ZnO and  $\text{Ti}_3\text{C}_2\text{T}_x$ , the presence of the independent characteristic diffraction peak of ZnO can be verified. Meanwhile, the characteristic diffraction peak of  $\text{Ti}_3\text{C}_2\text{T}_x$  appears at  $6.9^\circ$ , indicating that ZnO and  $\text{Ti}_3\text{C}_2\text{T}_x$  are successfully combined. Besides, the relative diffraction peak intensity of  $\text{Ti}_3\text{C}_2\text{T}_x$  decreases as the relative content of  $\text{Ti}_3\text{C}_2\text{T}_x$  decreases from 40 % (M3) to 25 % (M2) and then to 14 % (M1).

The micromorphology of the samples was investigated by SEM. Fig. 2 (a–d) show the SEM images of  $\text{Ti}_3\text{AlC}_2$  MAX phase, pure  $\text{Ti}_3\text{C}_2\text{T}_x$ , ZnO nanowires, and  $\text{Ti}_3\text{C}_2\text{T}_x/\text{ZnO}$  composite material, respectively. Fig. 2(e–f) show the SEM image of  $\text{Ti}_3\text{C}_2\text{T}_x/\text{ZnO}$  composite material at high magnification. It is clear from Fig. 2(a–b) that the  $\text{Ti}_3\text{AlC}_2$  layers are tightly adhered together without stratification. After etching, the

spacing between the layers becomes significantly larger, resembling a typical open stacked sheet structure (Han et al., 2020). This indicates that the Al atom layer in the  $\text{Ti}_3\text{AlC}_2$  precursor structure can be selectively etched by LiF + HCl system, resulting in a typical 2D accordion morphology, with obvious microscopic pores between the layers. Besides, it can be seen in Fig. 2(c) that the surface of ZnO nanowires is smooth and compact, with excellent crystallinity, and the dispersion is uniform. Fig. 2(e–g) show that the 1D ZnO nanowires are uniformly distributed on the surface and between the layers of 2D  $\text{Ti}_3\text{C}_2\text{T}_x$ . The composite samples have a 2D layered structure, where the ZnO nanowires are inserted in the 2D layered structure of  $\text{Ti}_3\text{C}_2\text{T}_x$ , indicating the successful synthesis of  $\text{Ti}_3\text{C}_2\text{T}_x/\text{ZnO}$ . EDS elemental mapping was employed to reveal the spatial distribution of elements in the as-formed  $\text{Ti}_3\text{C}_2\text{T}_x/\text{ZnO}$ , as shown in Fig. 2(h–i). It is shown that the C, O, Ti, and Zn elements are uniformly distributed throughout the heterostructures. It is showed that the surface of  $\text{Ti}_3\text{C}_2\text{T}_x$  sample formed through etching by LiF + HCl has –O and –F functional groups, while the nanowires on the surface of sheet structure are ZnO, which is consistent with the results of SEM and TEM.

The microstructure and internal crystal structure of the  $\text{Ti}_3\text{C}_2\text{T}_x/\text{ZnO}$  composite were examined by HRTEM. Fig. 3(a) shows that the ZnO nanowires are uniformly distributed on the surface and between the layers of  $\text{Ti}_3\text{C}_2\text{T}_x$ , which is consistent with the SEM results. Fig. 3(c) presents the HRTEM image of the composite, where the lattice fringe spacings of 0.26 and 0.307 nm are attributed to the (002) plane of ZnO and the (002) plane of  $\text{Ti}_3\text{C}_2\text{T}_x$ , respectively. These results are consistent with the previous characterizations.

The specific surface area and pore structure of  $\text{Ti}_3\text{C}_2\text{T}_x/\text{ZnO}$  and  $\text{Ti}_3\text{C}_2\text{T}_x$  samples were analyzed by  $\text{N}_2$  adsorption–desorption isotherm measurement. The results are shown in Fig. 4. The isotherm reveals a H3-type hysteresis loop at a relative pressure ( $P/P_0$ ) of 0.7–1.0, indicating that the samples have an obvious mesoporous structure. The BET specific surface area of M1, M2 and M3 are calculated to be 23.92, 24.22 and 24.75  $\text{m}^2/\text{g}$ , respectively. The difference among M1, M2 and M3 is very small. This indicates that the effect of the difference in titanium carbide content in the composites on the specific surface area is minimal.

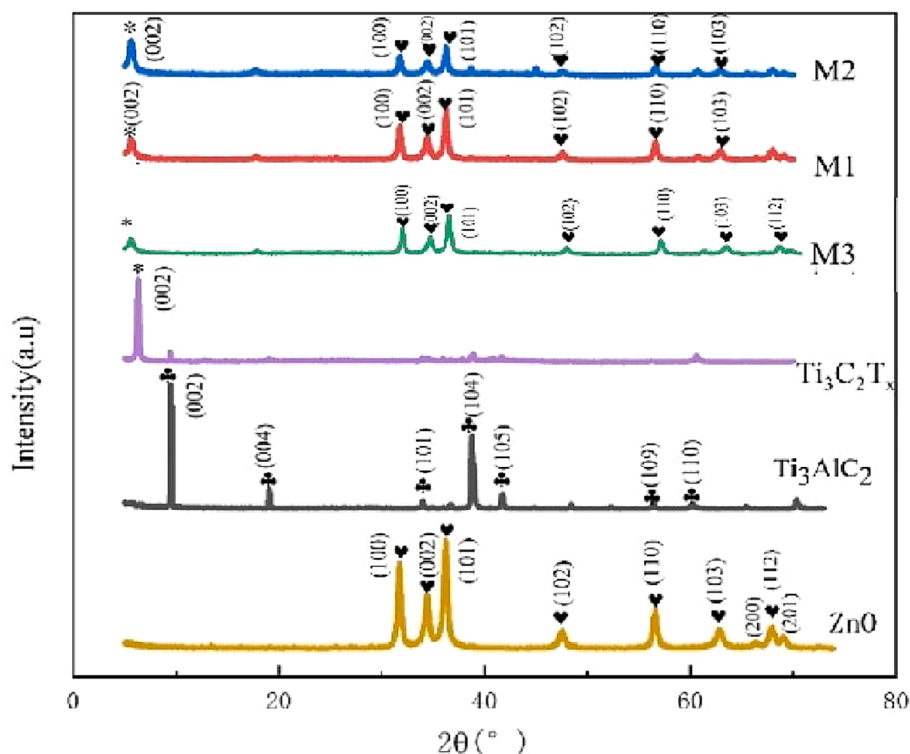
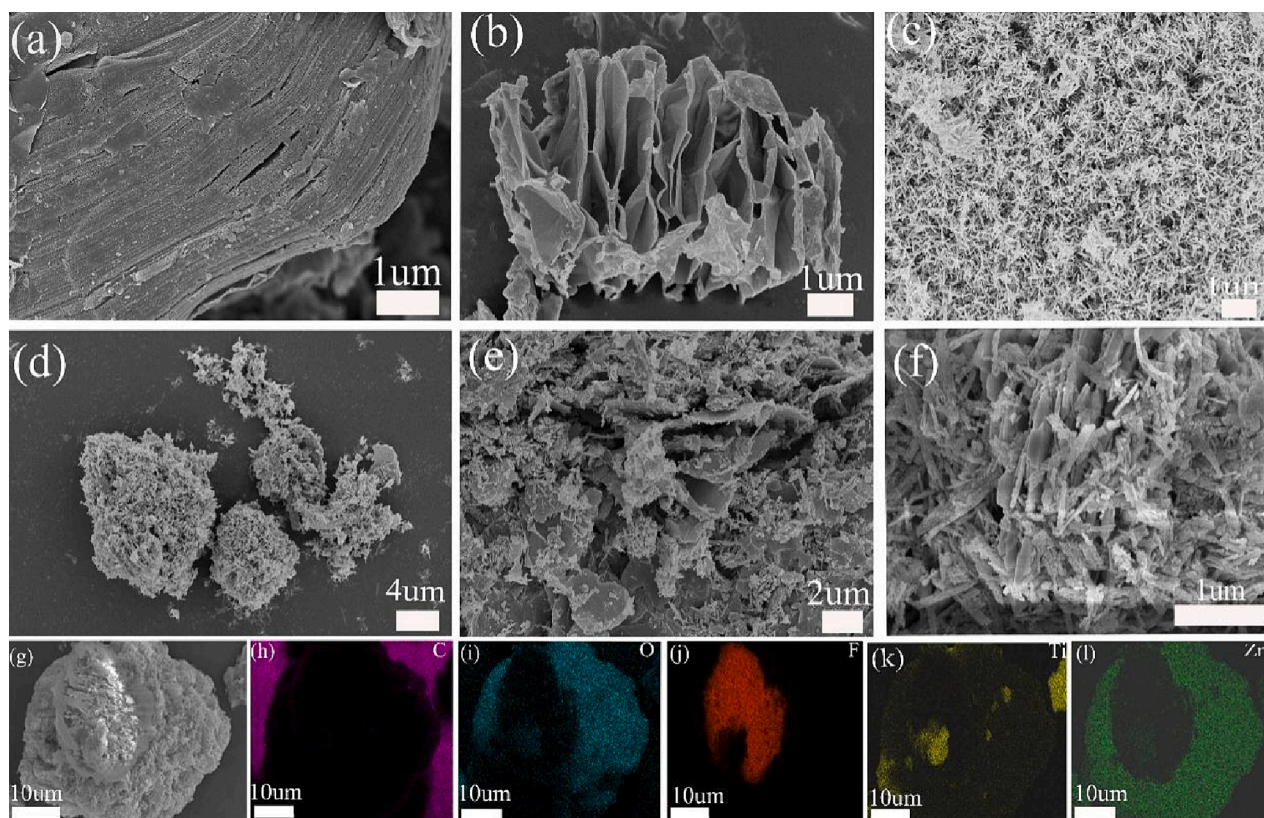
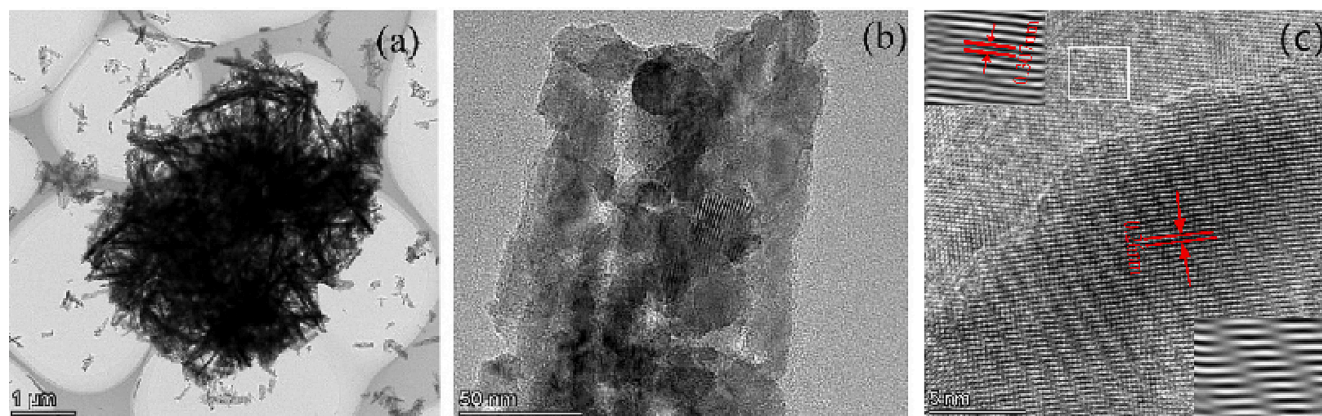


Fig. 1. XRD patterns of  $\text{Ti}_3\text{AlC}_2$ ,  $\text{Ti}_3\text{C}_2\text{T}_x$  MXene sheets, ZnO nanowires, and M1, M2 and M3 composite materials.



**Fig. 2.** SEM images of (a)  $\text{Ti}_3\text{AlC}_2$  MAX phase; (b) pure  $\text{Ti}_3\text{C}_2\text{T}_x$  nanosheets; (c) ZnO nanowires; (d-g)  $\text{Ti}_3\text{C}_2\text{T}_x/\text{ZnO}$  composite materials. (h-l) EDS mapping analysis of C, O, F, Ti, and Zn.



**Fig. 3.** (a-b) TEM image of the synthesized  $\text{Ti}_3\text{C}_2\text{T}_x/\text{ZnO}$  composites from different perspectives; (c) HRTEM image showing the interlayer spacing of the synthesized  $\text{Ti}_3\text{C}_2\text{T}_x/\text{ZnO}$  composites.

The BET specific surface area of M is calculated to be  $7.2923 \text{ m}^2/\text{g}$ . This implies that the specific surface area of the  $\text{Ti}_3\text{C}_2\text{T}_x/\text{ZnO}$  composite material is nearly three times higher than that of  $\text{Ti}_3\text{C}_2\text{T}_x$ , indicating the potential of the proposed structure in gas sensing application.

XPS was used to examine the elemental composition and chemical state of different materials. Fig. 5(a) shows the full survey spectrum of ZnO, where only Zn, O, and C elements can be observed. This confirms a high purity of the ZnO nanowires. The high-resolution XPS spectrum of Zn 2p in Fig. 5(b) shows two strong peaks at 1021.8 and 1044.9 eV, which are attributed Zn 2p<sub>3/2</sub> and Zn 2p<sub>1/2</sub>, respectively, indicating the normal oxidation state of  $\text{Zn}^{2+}$  in ZnO nanowires (Zhao et al., 2021). Besides, the spacing between the two Zn 2p peaks is 23.1 eV, which is consistent with the energy splitting of ZnO. Fig. 5(c) shows the high-

resolution XPS spectrum of O1s, where the peak at 529.53 eV can be assigned to  $\text{O}^{2-}$  in ZnO nanowires, while the peak at 530.28 eV is ascribed to the surface hydroxyl group formed due to the reaction of chemisorbed oxygen with water in the atmosphere (Zhao et al., 2019). Fig. 5(d) shows the full survey spectrum of  $\text{Ti}_3\text{C}_2\text{T}_x$ . It is evident that the  $\text{Ti}_3\text{C}_2\text{T}_x$  sheets are composed of Ti, C, O, and F elements. The spectra of individual elements was verified by Gaussian fitting. In the fitted C 1 s spectrum, there are four peaks at the binding energies of 280.63, 283.58, 284.33, and 288.28 eV, which can be indexed to C-Ti, C-C, C-O, and  $\text{CH}_x$ -C-O bonds (Halim et al., 2016; Wu et al., 2017), respectively, proving a typical carbon bonding in  $\text{Ti}_3\text{C}_2\text{T}_x$  MXene. As shown in Fig. 5(e), the Ti 2p XPS spectra of  $\text{Ti}_3\text{C}_2\text{T}_x$  can be divided into six peaks at the binding energies of 453.9, 454.98, 458.23, 460.18, and 464.8 eV, which

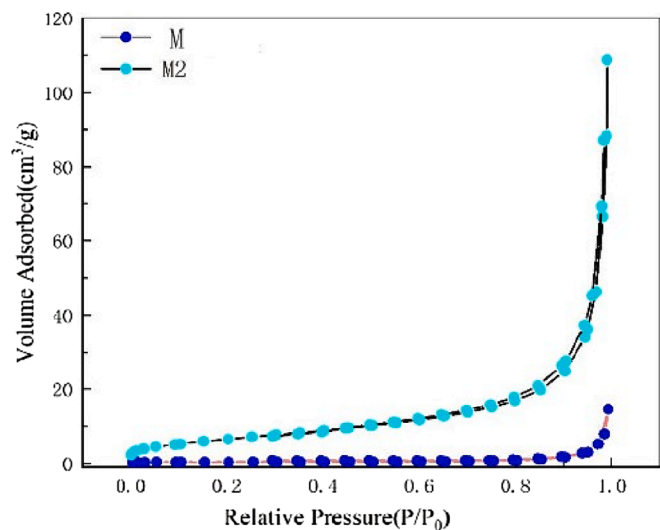


Fig. 4.  $N_2$  adsorption-desorption isotherms of  $Ti_3C_2T_x$  (M) and  $Ti_3C_2T_x/ZnO$  composite.

correspond to  $Ti-C(Ti^{2+})$ ,  $Ti-X(Ti^{3+})$ ,  $TiO_2-X-F_x$ ,  $C-Ti-F_x$ , and  $TiO_2(Ti^{4+})$ , respectively (Halim et al., 2014). Fig. 5(g) shows the full survey spectrum of  $Ti_3C_2T_x/ZnO$  composite. The characteristic peaks of Ti, O, C, Z, and F can be observed in the full spectrum, which is consistent with the EDS mapping results. The C 1s spectra shows three peaks corresponding to different carbon bonds: C-O, C-C, and C-Ti- $T_x$ . The fitted Ti 2p spectra shows four different peaks, which represent C-Ti- $O_xF_x$ , Ti-C, C-Ti- $O_x$ , and C-Ti- $F_x$ ,  $TiO_2$ . However, compared to the Ti 2p spectrum of  $Ti_3C_2T_x$ , the area of C-Ti- $F_x$  peak is significantly decreased because the attached ZnO has added the oxygen terminal to  $Ti_3C_2T_x$ .

### 3.2. Gas-sensing properties

To determine the optimal operating temperature of composites and  $Ti_3C_2T_x/ZnO$  pure  $Ti_3C_2T_x$ , the sensing response of the samples M, M1, M2, and M3 to 100 ppm  $NO_2$  at different operating temperatures was examined, and the results are shown in Fig. 6(a). As the operating temperature increases, the response values of M, M1, M2, and M3 gas sensors first increase and then decrease. The response of all the samples becomes maximum at 250 °C. Specifically, the maximum response values of M, M1, M2, and M3 to 100 ppm  $NO_2$  are 4.3, 17.07, 18.66, and 8.5, respectively. Therefore, 250 °C is selected as the optimal operating temperature of all the sensors. Fig. 6(b) shows the dynamic response-

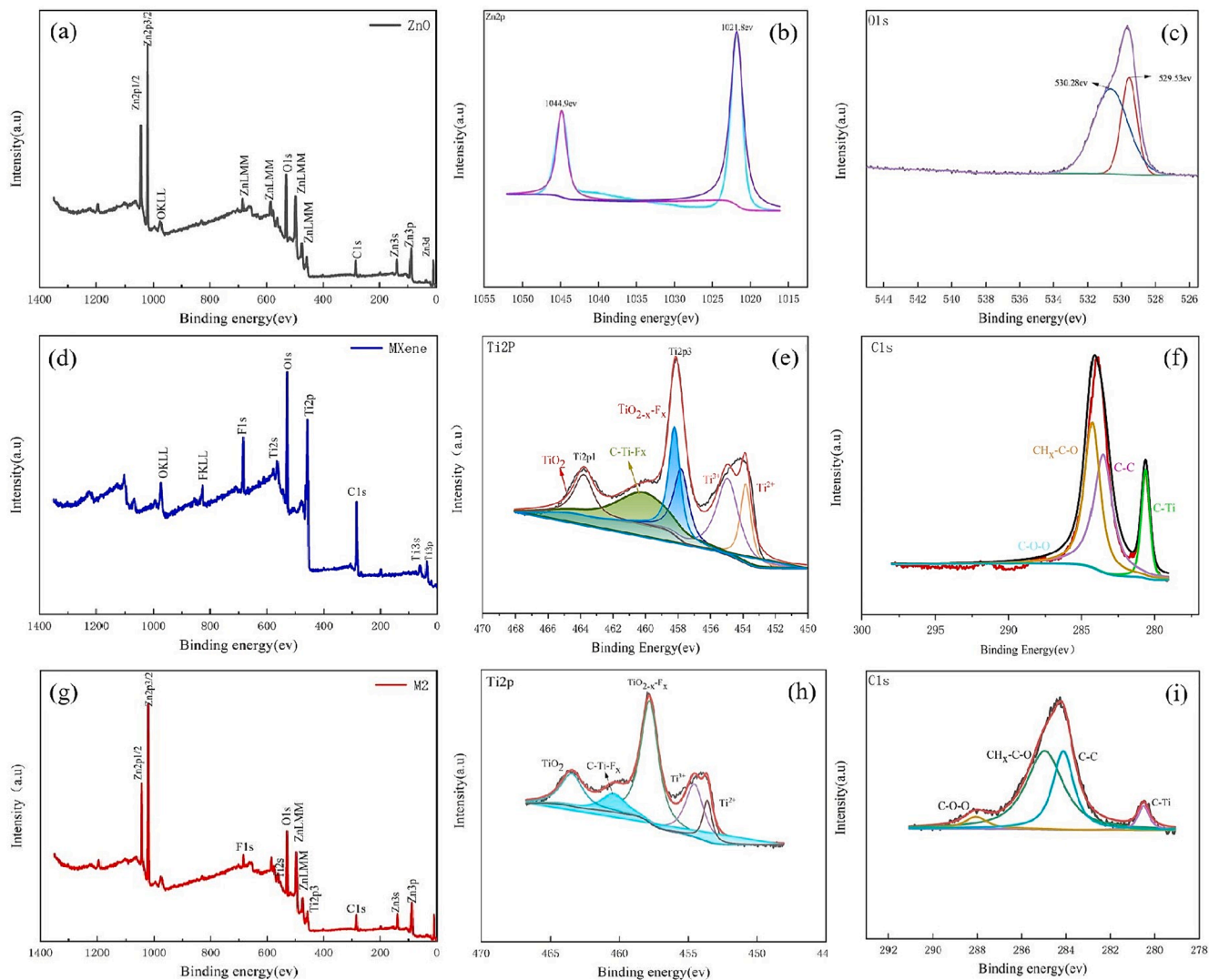
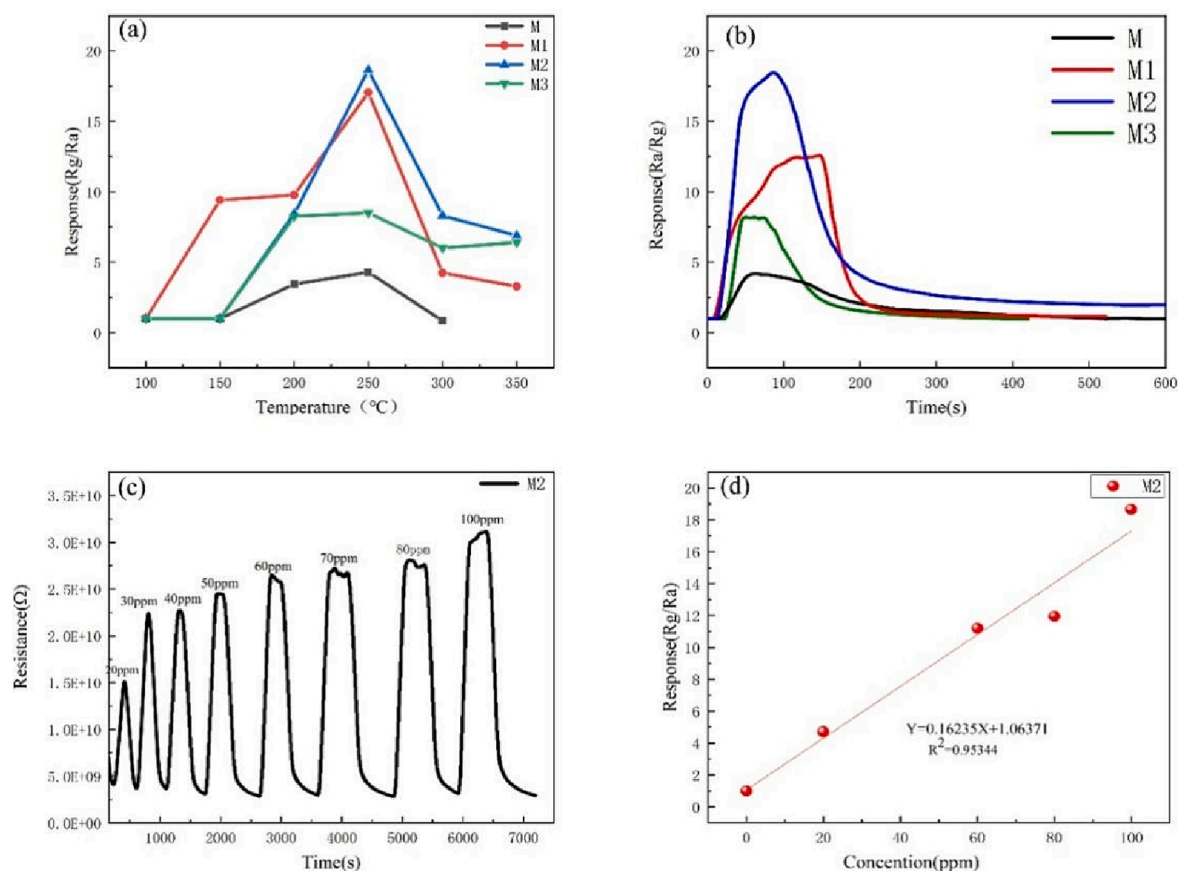


Fig. 5. (a) XPS full survey spectrum of ZnO; XPS spectra of (b) Zn 2p and (c) C 1s for ZnO; (d) XPS full survey spectrum of  $Ti_3C_2T_x$ ; high-resolution XPS spectra of (e) Ti 2p and (f) C 1s for  $Ti_3C_2T_x$ ; (g) XPS full survey spectrum of  $Ti_3C_2T_x/ZnO$ ; high-resolution XPS spectra of (h) Ti 2p and (i) C 1s for  $Ti_3C_2T_x/ZnO$  composite.



**Fig. 6.** (a) Response of materials towards 100 ppm NO<sub>2</sub> at different temperatures. (b) Response-recovery of different materials to 100 ppm NO<sub>2</sub> at 250 °C. (c) Dynamic response-recovery curves for different NO<sub>2</sub> concentrations (20–100 ppm) at 250 °C. (d) Linear fitting of the response curve of Ti<sub>3</sub>C<sub>2</sub>T<sub>x</sub>/ZnO composite to 0–100 ppm NO<sub>2</sub> at 250 °C.

recovery curves of different sensors at the optimal operating working temperature. It is evident that the response value of all the composite materials is higher than that of the pure Ti<sub>3</sub>C<sub>2</sub>T<sub>x</sub>. The response of sample M2 reaches a maximum of 18.66. Specifically, compared to the pure-Ti<sub>3</sub>C<sub>2</sub>T<sub>x</sub>, the sensitivity of Ti<sub>3</sub>C<sub>2</sub>T<sub>x</sub>/ZnO composite is enhanced by almost 4.3 times. Further, within the range of 100 s, the sensitivity of the four different sensor materials rises rapidly. The M2 is determined to represent the best gas-sensing performances of Ti<sub>3</sub>C<sub>2</sub>T<sub>x</sub>/ZnO composites in the future measurements. Moreover, all of the responses of these sensors based on Ti<sub>3</sub>C<sub>2</sub>T<sub>x</sub>/ZnO composites are much higher than that of their pristine components, indicating that the gas-sensing performances can be improved by the pure Ti<sub>3</sub>C<sub>2</sub>T<sub>x</sub>. Fig. 6(c) shows that the sensor exhibits extremely high sensitivity for ppm-level NO<sub>2</sub> gas at 250 °C. In particular, the response of the Ti<sub>3</sub>C<sub>2</sub>T<sub>x</sub>/ZnO composite shows a good linear relationship with the NO<sub>2</sub> concentration ( $R^2 = 0.95344$ ), which indicates that the Ti<sub>3</sub>C<sub>2</sub>T<sub>x</sub>/ZnO composite-based sensor can be used for real-time detection of NO<sub>2</sub> gas. Fig. 6(d) shows that good linear fits are also acquired. The limit of detection (LOD) of the sensor based on the Ti<sub>3</sub>C<sub>2</sub>T<sub>x</sub>/ZnO composite is estimated to be 0.105 ppm based on the equation  $LOD = 3\sigma_D/\sigma$  (here,  $\sigma_D$  is the standard deviation of noise during the response and  $\sigma$  is the slope of the linear part).

Repeatability and long-term stability are the two primary performance indicators for the practical application of a gas sensor. The repeatability of a gas sensor is measured by changing the gas concentration. Fig. 7(a) shows the dynamic resistance vs. time curve of the M2 composite sample for five cycles under exposure to 100 ppm NO<sub>2</sub>. The M2 composite shows an excellent repeatability without any significant attenuation in the response under alternate exposure to air and 100 ppm NO<sub>2</sub>. Furthermore, Fig. 7(b) shows the response of Ti<sub>3</sub>C<sub>2</sub>T<sub>x</sub>/ZnO composite exposed to 100 ppm NO<sub>2</sub> for a continuous 30 days. The test was

performed once every 5 days for 6 consecutive times, and the results show a slight fluctuation or negligible reduction, indicating good long-term stability. At the optimal operating temperature, the response and recovery curves of samples M and M2 exposed to 100 ppm NO<sub>2</sub> are shown in Fig. 7(c,d). After NO<sub>2</sub> gas is injected, the response of samples M and M1 increases rapidly and becomes stable at the maximum value. The response time and recovery time of M2 are calculated to be 17 and 102 s, respectively, which are both lower than those of Ti<sub>3</sub>C<sub>2</sub>T<sub>x</sub> gas sensor. The results demonstrate that the Ti<sub>3</sub>C<sub>2</sub>T<sub>x</sub>/ZnO composite-based sensor exhibits a comparatively fast response/recovery to NO<sub>2</sub> gas at 250 °C. Besides, it can be seen that the sensor cannot fully recover to its initial resistance. This may be because the sensor measures the concentration of target gas at a high temperature, and a certain amount of residual NO<sub>2</sub> gas molecules are adsorbed on the sample, occupying the effective adsorption sites of oxygen, which inevitably reduces the recovery resistance value. The improvement in the gas sensitivity of Ti<sub>3</sub>C<sub>2</sub>T<sub>x</sub> can be ascribed to the formation of heterojunction between Ti<sub>3</sub>C<sub>2</sub>T<sub>x</sub> and ZnO (Wang et al., 2022). The good conductive network provided by 2DTi<sub>3</sub>C<sub>2</sub>T<sub>x</sub> can greatly enhance the mobility of free charge carriers in the gas–solid reaction process, improve the reaction rate at the gas–solid interface, facilitate the gas adsorption, and shorten the response/recovery time.

Selectivity is an important characteristic of gas sensors. To evaluate the ability of the gas sensor to recognize NO<sub>2</sub> and avoid the interference of background gases, the selectivity of Ti<sub>3</sub>C<sub>2</sub>T<sub>x</sub>/ZnO composites was tested. Fig. 8 shows the response of Ti<sub>3</sub>C<sub>2</sub>T<sub>x</sub>/ZnO composite-based sensor to six different gases (ethanol, acetone, acetaldehyde, methanol, NO<sub>2</sub> and SO<sub>2</sub>) at the optimal operating temperature of 250 °C. The gas response values of M2 sensor to 1000 ppm ethanol, acetone, acetaldehyde, and methanol are 0, 0, 1.94, and 0.86, respectively. The gas

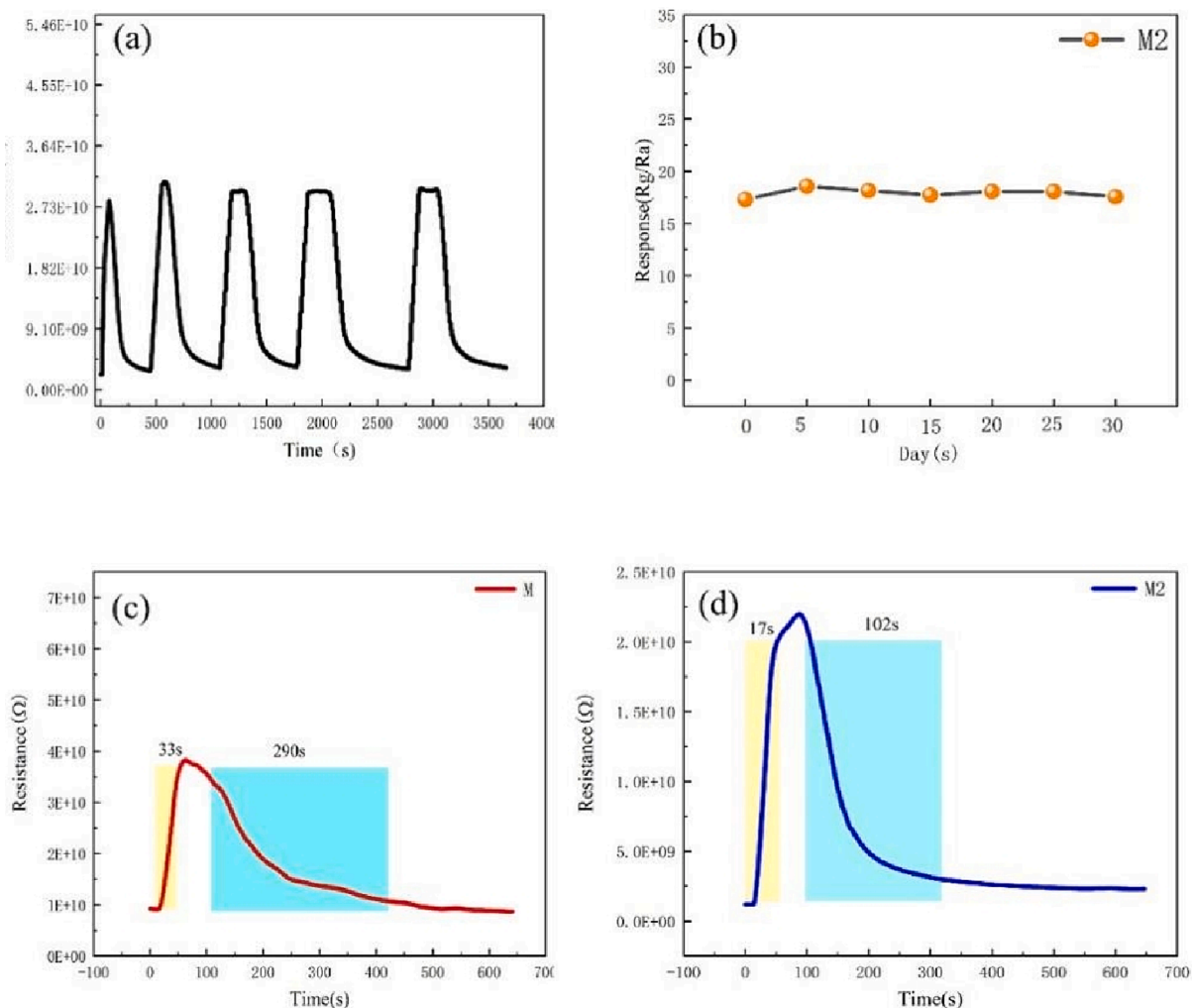


**Fig. 7.** (a) Cyclic transient sensing response towards 100 ppm NO<sub>2</sub>; (b) long-term stability of Ti<sub>3</sub>C<sub>2</sub>T<sub>x</sub>/ZnO composite; (c-d) response and recovery time of the sensors based on M and M2 composites to 100 ppm NO<sub>2</sub> at 250 °C.

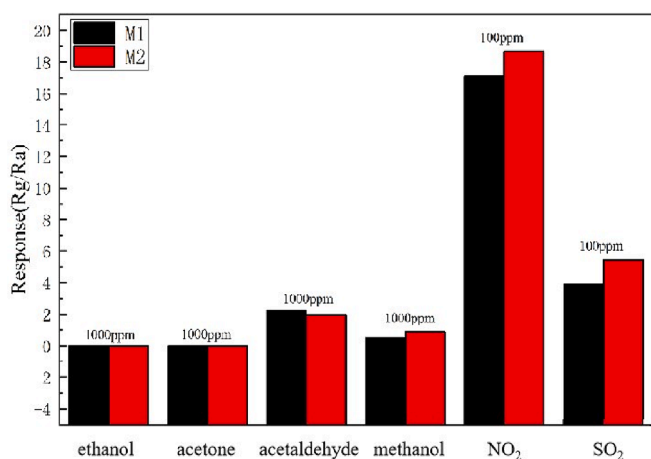


**Fig. 8.** Selectivity of Ti<sub>3</sub>C<sub>2</sub>T<sub>x</sub>/ZnO composite to various target gases.

response values of M1 and M2 sensors to 100 ppm SO<sub>2</sub> are 3.87 and 5.02. Thus, the response of Ti<sub>3</sub>C<sub>2</sub>T<sub>x</sub>/ZnO composite-based sensor to NO<sub>2</sub> is much higher than that to other gases, indicating its excellent selectivity to NO<sub>2</sub>. This suggests that the M1 and M2 gas sensitive elements show good response and selectively toward NO<sub>2</sub> in the presence of several

background gases.

### 3.3. Gas sensing mechanism

Herein, a possible mechanism for the gas sensing property of Ti<sub>3</sub>C<sub>2</sub>T<sub>x</sub>/ZnO composite material is established based on the modulation of depletion layer. After the contact in vacuum, the charge carrier transfer process occurs at the Ti<sub>3</sub>C<sub>2</sub>T<sub>x</sub> interface due to the difference in Fermi energy and then stops until the static charge equilibrium is reached when the Fermi level ( $E_f$ ) flattens under the action of internal electric field, causing band bending, as shown in Fig. 9(c). When the Ti<sub>3</sub>C<sub>2</sub>T<sub>x</sub>/ZnO gas sensor is exposed to air, O<sub>2</sub> molecules can not only capture free electrons from the conduction band of ZnO and convert them into O<sup>2-</sup>, but also obtain electrons from Ti<sub>3</sub>C<sub>2</sub>T<sub>x</sub> through surface functional groups (-OH and -O, -F) to produce O<sup>2-</sup>. The adsorbed O<sup>2-</sup> ions can further gain electrons to form O<sup>-</sup> ions, causing an increase in the Schottky barrier and the formation of electron depletion layer (Su et al., 2019), as shown in Fig. 9(d). When the Ti<sub>3</sub>C<sub>2</sub>T<sub>x</sub>/ZnO gas sensor is exposed to NO<sub>2</sub>, which is a typical oxidizing gas with high electron affinity, NO<sub>2</sub> can be adsorbed on surface of Ti<sub>3</sub>C<sub>2</sub>T<sub>x</sub>/ZnO composite and capture electrons form NO<sup>2-</sup>. The depletion layer at the interface widens, and the resistance increases, as shown in Fig. 9(e). As NO<sub>2</sub> further reacts with a large amount of O<sup>2-</sup> on the material surface to form NO<sup>2-</sup>, the ZnO conduction band and Ti<sub>3</sub>C<sub>2</sub>T<sub>x</sub> continue to lose electrons. Besides, the depletion layer further widens and the resistance increases,

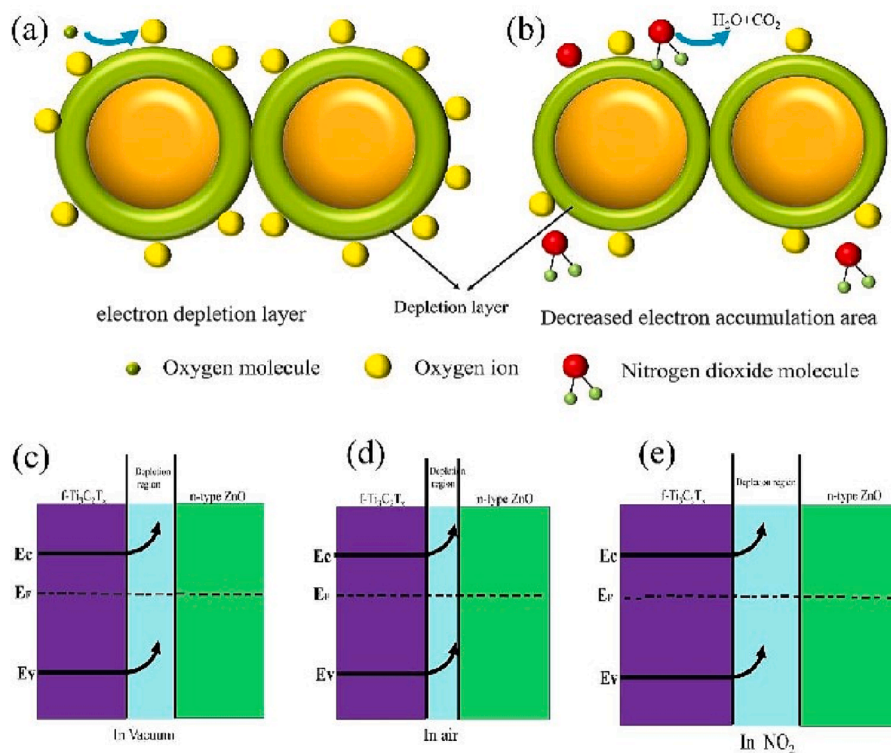


Fig. 9. (a-b) Schematic illustration of the  $\text{NO}_2$  gas sensing mechanism of  $\text{Ti}_3\text{C}_2\text{T}_x/\text{ZnO}$  nanocomposite. Schottky barrier in (c) vacuum, (d) air, and (e)  $\text{NO}_2$ .

and the adsorbed  $\text{O}^-$  ions on the surface of ZnO spheres also play a major part in the chemical adsorption of  $\text{NO}_2$  (Yang et al., 2016; Al-hadeethi et al., 2017).

#### 4. Conclusions

The  $\text{Ti}_3\text{C}_2\text{T}_x/\text{ZnO}$  nanocomposites were successfully synthesized through the electrostatic self-assembly method. The microstructure of the composites with different contents of  $\text{Ti}_3\text{C}_2\text{T}_x$  were analyzed. Furthermore, the optimal operating temperature, concentration, stability, response and recovery time, and selectivity of the  $\text{Ti}_3\text{C}_2\text{T}_x/\text{ZnO}$  composite-based gas sensor to  $\text{NO}_2$  gas were investigated. The  $\text{Ti}_3\text{C}_2\text{T}_x/\text{ZnO}$  nanocomposites containing 25 %  $\text{Ti}_3\text{C}_2\text{T}_x$  exhibited the best  $\text{NO}_2$  sensing performance with a response value of 18.66, fast response and recovery (17/102 s), and outstanding selectivity compared to pure  $\text{Ti}_3\text{C}_2\text{T}_x$ . The response of  $\text{Ti}_3\text{C}_2\text{T}_x/\text{ZnO}$  nanocomposites toward 100 ppm  $\text{NO}_2$  gas was almost 4.3 times higher than that of pure  $\text{Ti}_3\text{C}_2\text{T}_x$ , which could be ascribed to the preferred surface termination group, large specific surface area of  $\text{Ti}_3\text{C}_2\text{T}_x$ , and heterogeneous structure constructed by ZnO and  $\text{Ti}_3\text{C}_2\text{T}_x$ .

#### CRediT authorship contribution statement

**Jiyun Gao:** Data curation, Investigation, Methodology, Writing – original draft, Writing – review & editing. **Youyou Yin:** Data curation, Formal analysis. **Yongjing Guo:** Data curation, Formal analysis. **Lijuan Jia:** Data curation, Investigation. **Futing Xia:** Data curation, Formal analysis, Writing – review & editing. **Chenhui Liu:** Funding acquisition, Supervision. **Ming Hou:** Formal analysis, Investigation. **Fang Wang:** Supervision, Writing – original draft.

#### Declaration of Competing Interest

The authors declare that they have no known competing financial interests or personal relationships that could have appeared to influence the work reported in this paper.

#### Acknowledgments

This research was funded by National Natural Science Foundation of China, No.52304400; Youth Fund Project of Yunnan Province, No.202201AU070156; Ten Thousand Talent Plans for Young Top-notch Talents of Yunnan Province (YNWR-QNBJ-2019-066).

#### References

- Al-Hadeethi, Y., Umar, A., Ibrahim, A.A., Al-Heniti, S.H., Kumar, R., Baskoutas, S., Raffah, B.M., 2017. Synthesis, characterization and acetone gas sensing applications of Ag-doped ZnO nanoneedles. *Ceramics International*. 43, 6765–6770. <https://doi.org/10.1016/j.ceramint.2017.02.088>.
- Bhowmick, T., Ghosh, A., Nag, S., Majumder, S.B., 2022. Sensitive and selective  $\text{CO}_2$  gas sensor based on CuO/ZnO bilayer thin-film architecture. *Journal of Alloys and Compounds*. 903, 163871 <https://doi.org/10.1016/j.jallcom.2022.163871>.
- Chen, X., Shen, Y., Zhang, W., Zhang, J., Wei, D., Lu, R., Zhu, L., Li, H., 2018. In-situ growth of ZnO nanowire arrays on the sensing electrode via a facile hydrothermal route for high-performance  $\text{NO}_2$  sensor. *APPLIED SURFACE SCIENCE*. 435, 1096–1104. <https://doi.org/10.1016/j.apsusc.2017.11.222>.
- Fan, C., Shi, J., Zhang, Y., Quan, W., Chen, X., Yang, J., Zeng, M., Zhou, Z., Su, Y., Wei, H., 2022. Fast and recoverable  $\text{NO}_2$  detection achieved by assembling ZnO on  $\text{Ti}_3\text{C}_2\text{T}_x$  MXene nanosheets under UV illumination at room temperature. *Nanoscale*. 14, 3441–3451. <https://doi.org/10.1039/D1NR06838E>.
- Fan, Z., Wang, Y., Xie, Z., Xu, X., Yuan, Y., Cheng, Z., Liu, Y., 2018. A nanoporous MXene film enables flexible supercapacitors with high energy storage. *Nanoscale*. 10, 9642–9652. <https://doi.org/10.1039/C8NR01550C>.
- Gogotsi, Y., Anasori, B., 2019. The rise of MXenes. *ACS Publications*. 8491–8494 <https://doi.org/10.1021/acsnano.9b06394>.
- Gong, X., Yu, L., Tian, G., Wang, L., Zhao, Y., Mai, W., Wang, W., 2014. Synthesis and characterization of flower-like ZnO nanostructures via flower-like ZnOHf intermediate. *Materials Letters*. 127, 36–39. <https://doi.org/10.1016/j.matlet.2014.04.071>.
- Halim, J., Lukatskaya, M.R., Cook, K.M., Lu, J., Smith, C.R., Näslund, L.-Å., May, S.J., Hultman, L., Gogotsi, Y., Eklund, P., 2014. Transparent conductive two-dimensional titanium carbide epitaxial thin films. *Chemistry of Materials*. 26, 2374–2381. <https://doi.org/10.1021/cm500641a>.
- Halim, J., Cook, K.M., Naguib, M., Eklund, P., Gogotsi, Y., Rosen, J., Barsoum, M.W., 2016. X-ray photoelectron spectroscopy of select multi-layered transition metal carbides (MXenes). *APPLIED SURFACE SCIENCE*. 362, 406–417. <https://doi.org/10.1016/j.apsusc.2015.11.089>.
- Han, M., Shuck, C.E., Rakhmanov, R., Parchment, D., Anasori, B., Koo, C.M., Friedman, G., Gogotsi, Y., 2020. Beyond  $\text{Ti}_3\text{C}_2\text{T}_x$ : MXenes for electromagnetic

- interference shielding. *ACS Nano*. 14, 5008–5016. <https://doi.org/10.1021/acsnano.0c01312>.
- He, T., Liu, W., Lv, T., Ma, M., Liu, Z., Vasiliev, A., Li, X., 2021. MXene/SnO<sub>2</sub> heterojunction based chemical gas sensors. *Sensors and Actuators b: Chemical*. 329, 129275 <https://doi.org/10.1016/j.snb.2020.129275>.
- Hou, M., Gao, J., Yang, L., Guo, S., Hu, T., Li, Y., 2021. Room temperature gas sensing under UV light irradiation for Ti<sub>3</sub>C<sub>2</sub>T<sub>x</sub> MXene derived lamellar TiO<sub>2</sub>-C/g-C<sub>3</sub>N<sub>4</sub> composites. *APPLIED SURFACE SCIENCE*. 535, 147666 <https://doi.org/10.1016/j.apsusc.2020.147666>.
- Kanda, K., Maekawa, T., 2005. Development of a WO<sub>3</sub> thick-film-based sensor for the detection of VOC. *Sensors and Actuators b: Chemical*. 108, 97–101. <https://doi.org/10.1016/j.snb.2005.01.038>.
- Keerthana, S., Rathnakannan, K., 2022. Hierarchical ZnO/CuO nanostructures for room temperature detection of carbon dioxide. *Journal of Alloys and Compounds*. 897, 162988 <https://doi.org/10.1016/j.jallcom.2021.162988>.
- Kim S. J., Koh H.-J., Ren C. E., Kwon O., Maleski K., Cho S.-Y., Anasori B., Kim C.-K., Choi Y.-K., Kim J., 2018. Metallic Ti<sub>3</sub>C<sub>2</sub>T<sub>x</sub> MXene gas sensors with ultrahigh signal-to-noise ratio. *ACS nano*. 12, 986–993. <https://doi.org/10.1021/acsnano.7b07460>.
- Lee, E., VahidMohammadi, A., Yoon, Y.S., Beidaghi, M., Kim, D.-J., 2019. Two-dimensional vanadium carbide MXene for gas sensors with ultrahigh sensitivity toward nonpolar gases. *ACS Sensors*. 4, 1603–1611. <https://doi.org/10.1021/acssensors.9b00303>.
- Li, Y., Deng, X., Tian, J., Liang, Z., Cui, H., 2018. Ti<sub>3</sub>C<sub>2</sub> MXene-derived Ti<sub>3</sub>C<sub>2</sub>/TiO<sub>2</sub> nanoflowers for noble-metal-free photocatalytic overall water splitting. *Applied Materials Today*. 13, 217–227. <https://doi.org/10.1016/j.apmt.2018.09.004>.
- Li M., Lu J., Luo K., Li Y., Chang K., Chen K., Zhou J., Rosen J., Hultman L., Eklund P., 2019. Element replacement approach by reaction with Lewis acidic molten salts to synthesize nanolaminated MAX phases and MXenes. *Journal of the American Chemical Society*. 141, 4730–4737. <https://doi.org/10.1021/jacs.9b00574>.
- Li, X., Ran, F., Yang, F., Long, J., Shao, L., 2021. Advances in MXene films: synthesis, assembly, and applications. *Transactions of Tianjin University*. 27, 217–247. <https://doi.org/10.1007/s12209-021-00282-y>.
- Liu, F., Liu, Y., Zhao, X., Liu, X., Fan, L.Z., 2019. Pursuit of a high-capacity and long-life Mg-storage cathode by tailoring sandwich-structured MXene/carbon nanosphere composites. *Journal of Materials Chemistry a*. 7, 16712–16719. <https://doi.org/10.1039/C9TA02212K>.
- Liu, S., Wang, M., Ge, C., Lei, S., Hussain, S., Wang, M., Qiao, G., Liu, G., 2022. Enhanced room-temperature NO<sub>2</sub> sensing performance of SnO<sub>2</sub>/Ti<sub>3</sub>C<sub>2</sub> composite with double heterojunctions by controlling co-exposed and facets of SnO<sub>2</sub>. *Sensors and Actuators b: Chemical*. 365, 131919 <https://doi.org/10.1016/j.snb.2022.131919>.
- Naguib, M., Kurtoglu, M., Presser, V., Lu, J., Niu, J., Heon, M., Hultman, L., Gogotsi, Y., Barsoum, M.W., 2011a. Two-dimensional nanocrystals produced by exfoliation of Ti<sub>3</sub>AlC<sub>2</sub>. *ADVANCED MATERIALS*. 23, 4248–4253. <https://doi.org/10.1002/adma.201102306>.
- Naguib, M., Presser, V., Tallman, D., Lu, J., Hultman, L., Gogotsi, Y., Barsoum, M.W., 2011b. On the topotactic transformation of Ti<sub>2</sub>AlC into a Ti–C–O–F cubic phase by heating in molten lithium fluoride in air. *Journal of the American Ceramic Society*. 94, 4556–4561. <https://doi.org/10.1111/j.1551-2916.2011.04896.x>.
- Naguib, M., Mashtalir, O., Carle, J., Presser, V., Lu, J., Hultman, L., Gogotsi, Y., Barsoum, M.W., 2012. Two-Dimensional Transition Metal Carbides. *ACS Nano*. 6, 1322–1331. <https://doi.org/10.1021/nm204153h>.
- Orangi, J., Beidaghi, M., 2020. A Review of the Effects of Electrode Fabrication and Assembly Processes on the Structure and Electrochemical Performance of 2D MXenes. *Advanced Functional Materials*. 30, 20053051–20053052. <https://doi.org/10.1002/adfm.202005305>.
- Pei, Y., Zhang, X., Hui, Z., Zhou, J., Huang, X., Sun, G., Huang, W., 2021. Ti<sub>3</sub>C<sub>2</sub>T<sub>x</sub> MXene for sensing applications: recent progress, design principles, and future perspectives. *ACS Nano*. 15, 3996–4017. <https://doi.org/10.1021/acsnano.1c00248>.
- Qiu M. Y., 2014. Investigation on the gas sensing properties of ZnO thin films. *Applied Mechanics and Materials*. 685, 144–148. <https://doi.org/10.4028/www.scientific.net/AMM.685.144>.
- Shuvo, S.N., Ulloa, G.A.M., Mishra, A., Chen, W.Y., Dongare, A.M., Stanciu, L.A., 2020. Sulfur-doped titanium carbide MXenes for room-temperature gas sensing. *ACS Sensors*. 5, 2915–2924. <https://doi.org/10.1021/acssensors.0c01287>.
- Srinivasan, P., Mehre, S., 2022. Zinc oxide nanoparticles from *Coriandrum sativum* as sensor for detection of n-butanol and nitric oxide gas. *Materials Today: Proceedings*. 151, 1760–1764. <https://doi.org/10.1016/j.matpr.2021.01.760> Get rights and content.
- Su, C., Zhang, L., Han, Y., Chen, X., Wang, S., Zeng, M., Hu, N., Su, Y., Zhou, Z., Wei, H., 2019. Glucose-assisted synthesis of hierarchical flower-like Co<sub>3</sub>O<sub>4</sub> nanostructures assembled by porous nanosheets for enhanced acetone sensing. *Sensors and Actuators b: Chemical*. 288, 699–706. <https://doi.org/10.1016/j.snb.2019.03.004>.
- Teterycz, H., Klimkiewicz, R., Łaniecki, M., 2004. Study on physico-chemical properties of tin dioxide based gas sensitive materials used in condensation reactions of n-butanol. *Applied Catalysis a: General*. 274, 49–60. <https://doi.org/10.1016/j.apcata.2004.05.034>.
- Wang, J., Lian, G., 2004. Hydrothermal synthesis and photoluminescence properties of ZnO nanowires. *Solid State Communications*. 132, 269–271. <https://doi.org/10.1016/j.ssc.2004.07.052>.
- Wang, Z., Wang, F., Hermawan, A., Asakura, Y., Hasegawa, T., Kumagai, H., Kato, H., Kakihana, M., Zhu, J., Yin, S., 2021. SnO-SnO<sub>2</sub> modified two-dimensional MXene Ti<sub>3</sub>C<sub>2</sub>T<sub>x</sub> for acetone gas sensor working at room temperature. *Journal of Materials Science & Technology*. 73, 128–138. <https://doi.org/10.1016/j.jmst.2020.07.040>.
- Wang, J., Yang, Y., Xia, Y., 2022. Mesoporous MXene/ZnO nanorod hybrids of high surface area for UV-activated NO<sub>2</sub> gas sensing in ppb-level. *Sensors and Actuators b: Chemical*. 353, 2022. <https://doi.org/10.1016/j.snb.2021.131087>.
- Wei, B.-Y., Hsu, M.-C., Su, P.-G., Lin, H.-M., Wu, R.-J., Lai, H.-J., 2004. A novel SnO<sub>2</sub> gas sensor doped with carbon nanotubes operating at room temperature. *Sensors & Actuators B Chemical*. 101, 81–89. <https://doi.org/10.1016/j.snb.2004.02.028>.
- Wu, Y., Nie, P., Wang, J., Dou, H., Zhang, X., 2017. Few-layer MXenes delaminated via high-energy mechanical milling for enhanced sodium-ion batteries performance. *ACS APPLIED MATERIALS & INTERFACES*. 9, 39610–39617. <https://doi.org/10.1021/acsmi.7b12155>.
- Yang, Z., Jiang, L., Wang, J., Liu, F., He, J., Liu, A., Lv, S., You, R., Yan, X., Sun, P., 2021. Flexible resistive NO<sub>2</sub> gas sensor of three-dimensional crumpled MXene Ti<sub>3</sub>C<sub>2</sub>T<sub>x</sub>/ZnO spheres for room temperature application. *Sensors and Actuators b: Chemical*. 326, 128828 <https://doi.org/10.1016/j.snb.2020.128828>.
- Yang, S., Liu, Y., Chen, W., Jin, W., Zhou, J., Zhang, H., Zakharova, G.S., 2016. High sensitivity and good selectivity of ultralong MoO<sub>3</sub> nanobelts for trimethylamine gas. *Sensors and Actuators b: Chemical*. 226, 478–485. <https://doi.org/10.1016/j.snb.2015.12.005>.
- Yuan, W., Yang, K., Peng, H., Li, F., Yin, F., 2018. A flexible VOCs sensor based on a 3D MXene framework with a high sensing performance. *Journal of Materials Chemistry a*. 6, 18116–18124. <https://doi.org/10.1039/C8TA06928J>.
- Zhao, L., Chen, Y., Li, X., Li, X., Lin, S., Li, T., Rumyantseva, M.N., Gaskov, A.M., 2019. Room temperature formaldehyde sensing of hollow SnO<sub>2</sub>/ZnO heterojunctions under UV-LED activation. *IEEE Sensors Journal*. 19, 7207–7214. <https://doi.org/10.1109/JSEN.2019.2916879>.
- Zhao, S., Shen, Y., Hao, F., Kang, C., Cui, B., Wei, D., Meng, F., 2021. P-n junctions based on CuO-decorated ZnO nanowires for ethanol sensing application. *APPLIED SURFACE SCIENCE*. 538, 148140 <https://doi.org/10.1016/j.apsusc.2020.148140>.
- Zheng, S., Sun, J., Hao, J., Sun, Q., Wan, P., Li, Y., Zhou, X., Yuan, Y., Zhang, X., Wang, Y., 2021. Engineering SnO<sub>2</sub> nanorods/ethylenediamine-modified graphene heterojunctions with selective adsorption and electronic structure modulation for ultrasensitive room-temperature NO<sub>2</sub> detection. *Nanotechnology*. 32, 155505 <https://doi.org/10.1088/1361-6528/abd657>.